The Astrophysical Journal Letters, 924:L21 (8pp), 2022 January 10 https://doi.org/10.3847/2041-8213/ac4027

Three-Dimensional Anisotropy and Scaling Properties of Solar Wind Turbulence at Kinetic Scales in the Inner Heliosphere: Parker Solar Probe Observations

J. Zhang[1], S. Y. Huang[1], J. S. He[2], T. Y. Wang[3,4], Z. G. Yuan[1], X. H. Deng[5], K. Jiang[1], Y. Y. Wei[1], S. B. Xu[1], Q. Y. Xiong[1], R. T. Lin[1], and L. Yu[1]
[1] School of Electronic Information, Wuhan University, Wuhan, 430072, People's Republic of China; shiyonghuang@whu.edu.cn
[2] School of Earth and Space Sciences, Peking University, Beijing, 100871, People's Republic of China
[3] School of Earth Science, Yunnan University, Yunnan, 650091, People's Republic of China
[4] RAL Space, Rutherford Appleton Laboratory, Harwell Oxford, Didcot OX11 0QX, UK
[5] Insititute of Space Science and Technology, Nanchang University, Nanchang, 330031, People's Republic of China
Received 2021 September 2; revised 2021 December 2; accepted 2021 December 3; published 2022 January 11

Abstract

We utilize the data from the Parker Solar Probe mission at its first perihelion to investigate the three-dimensional (3D) anisotropies and scalings of solar wind turbulence for the total, perpendicular, and parallel magnetic-field fluctuations at kinetic scales in the inner heliosphere. By calculating the five-point second-order structure functions, we find that the three characteristic lengths of turbulence eddies for the total and the perpendicular magnetic-field fluctuations in the local reference frame ($\hat{L}_\perp$, $\hat{l}_\perp$, $\hat{l}_{||}$) defined with respect to the local mean magnetic field $\boldsymbol{B}_{\rm local}$ feature as $l_{||} > L_\perp > l_\perp$ in both the transition range and the ion-to-electron scales, but $l_{||} > L_\perp \approx l_\perp$ for the parallel magnetic-field fluctuations. For the total magnetic-field fluctuations, the wave-vector anisotropy scalings are characterized by $l_{||} \propto {l_\perp}^{0.78}$ and $L_\perp \propto {l_\perp}^{1.02}$ in the transition range, and they feature as $l_{||} \propto {l_\perp}^{0.44}$ and $L_\perp \propto {l_\perp}^{0.73}$ in the ion-to-electron scales. Still, we need more complete kinetic-scale turbulence models to explain all these observational results.

Unified Astronomy Thesaurus concepts: Solar wind (1534); Interplanetary turbulence (830)

1. Introduction

As a ubiquitous nonlinear phenomenon, turbulence acts to transfer dynamic energy from large scales to small scales, contributing significantly to particle acceleration and heating in astrophysical plasma (e.g., Tu & Marsch 1995; Bruno & Carbone 2005, 2013; Sahraoui et al. 2009, 2010, 2012, 2020; Huang & Sahraoui 2019; Huang et al. 2012, 2014, 2020a, 2020b; Wang et al. 2019). The solar wind provides a natural laboratory for in situ research of plasma turbulence with a power spectrum extending over many orders of scale and magnitude (e.g., Coleman 1968). Different scales of plasma turbulence can be characterized by distinct spectral indices. Scales between the outer scales and the ion characteristic scale are known as the inertial range or magnetohydrodynamic (MHD) scales, and the magnetic-field spectral index is observed to vary from $-5/3$ to $-3/2$ in the solar wind (e.g., Bruno & Carbone 2013; Chen et al. 2020) and from -2 to $-1/2$ in the Earth's magnetosheath (e.g., Huang et al. 2017). Below the MHD scales, sometimes a sharp transition range with spectral index up to -4 has been observed (Sahraoui et al. 2009, 2010, 2013; Kiyani et al. 2013; Bruno et al. 2014; He et al. 2015; Bowen et al. 2020a; Huang et al. 2014, 2017, 2020c, 2021). At smaller scales, a flatter power-law ion-to-electron scale forms with a spectral index that varies between -2.3 and -3.1 with a peak around -2.8 (Kiyani et al. 2013; Sahraoui et al. 2013; Huang et al. 2021).

Because the large-scale background magnetic field breaks the directional symmetry familiar in hydrodynamics (e.g., Osman et al. 2011), the solar wind turbulence shows many types of anisotropy (e.g., Horbury et al. 2012; Oughton et al. 2015; Parashar et al. 2016). At kinetic scales, numerous pioneering studies from different aspects (e.g., theoretical models, spacecraft observations, and numerical simulations) have been performed to reveal the anisotropy of solar wind turbulence.

In theory, the nature of the fluctuations determines the form of wave-vector anisotropy. The most relevant linear wave mode at kinetic scales of the solar wind has been confirmed to be the kinetic Alfvén wave (KAW), rather than the oblique magneto-sonic/whistler wave according to observational evidence (e.g., Sahraoui et al. 2009, 2010; He et al. 2011, 2012; Howes et al. 2012; Huang et al. 2020c). Based on the KAW turbulence model, Howes et al. (2008) and Schekochihin et al. (2009) proposed an anisotropy scaling of $k_{||} \propto {k_\perp}^{1/3}$. Here $k_{||}$ is the wave vector parallel to the background magnetic field and $k_\perp$ is the wave vector along with the perpendicular direction. Furthermore, many modified KAW models were also proposed. Such as, the phenomenological model which assumes that the turbulence consists of intermittent sheet-like structures predicted a scaling of $k_{||} \propto {k_\perp}^{2/3}$ (e.g., Boldyrev & Perez 2012). Zhao et al. (2016) considered the anisotropic dispersive effects and turbulent intermittency for the KAW turbulence, and inferred that the anisotropy scaling ranges from $1/3$ to $7/6$. Boldyrev & Loureiro (2019) speculated that the formation of strongly anisotropic structures is arrested by the tearing instability, and derived a corresponding spectral anisotropy between $k_{||} \propto {k_\perp}^{2/3}$ and $k_{||} \propto k_\perp$.

The kinetic-scale anisotropy of space plasma turbulence has also been reported in many observational studies from different spacecraft measurements, such as Cluster (e.g., Sahraoui et al. 2009, 2010; Chen et al. 2010; Comişel et al. 2014; Lacombe et al. 2017), the Magnetospheric MultiScale (MMS; e.g., Roberts et al. 2019; Wang et al. 2020), and PSP (e.g., Duan et al. 2021). Specifically, Sahraoui et al. (2010) displayed the anisotropic turbulence spectra for the first time by using the *k*-

filtering technique. Later, Chen et al. (2010) provided direct observation of turbulence anisotropy using a multispacecraft analysis technique. Wang et al. (2020) first presented a quantitative observation of 3D anisotropic properties at kinetic scales in the Earth's magnetosheath by measuring the five-point SFs of magnetic-field fluctuations. Most recently, Duan et al. (2021) reported the 2D anisotropy of the magnetic-field turbulence at kinetic scales by employing the methods of Morlet wavelet and five-point SF calculation to part of the PSP's first perihelion data. Their results manifested that there existed different anisotropic properties in the transition range and the ion-to-electron scales. Moreover, the power anisotropy near the PSP perihelion looks more evident than the results at 1 au. In addition, the wave modes of solar wind turbulence are also confirmed to be anisotropic at subion scales (He et al. 2011, 2015; Bowen et al. 2020b; Huang et al. 2020c).

Complementary to theories and observations, kinetic simulations have also attracted a lot of interest. Different anisotropy scaling relations at kinetic scales have also been proposed in solar wind turbulence simulations recently, such as, $k_{||} \propto k_{\perp}^{1/3}$ in Grošelj et al. (2018), $k_{||} \propto k_{\perp}^{2/3}$ in Cerri et al. (2019), $k_{||} \propto k_{\perp}^{(\alpha+1)/3}$ with α the coefficient proportional to the space filling of the turbulence in Landi et al. (2019), $k_{||} \propto k_{\perp}$ in Arzamasskiy et al. (2019), etc.

Limited by the distance of the spacecraft from the Sun, most of the previous observation results are unable to reveal the anisotropy of solar wind turbulence in the inner heliosphere. Launched on 2018 August 12, NASA's PSP spacecraft is expected to reach a minimum perihelion at 0.0459 au (~9.86 R_s, R_s is the solar radius), which can shed light on the physics of the nascent solar wind (e.g., Fox et al. 2016). Besides considering that the transition range has been frequently observed in the inner heliosphere (e.g., Bowen et al. 2020a; Huang et al. 2020c, 2021), PSP's observations can provide us with information on whether and how the 3D anisotropy and scaling of solar wind turbulence changes from the transition range to the ion-to-electron scales. This paper is organized as follows: we give a description of the data and the method in Section 2, the results are presented in Section 3, and finally, we summarize and discuss our results in Section 4.

2. Data and Methods

In this study, the data are from the first perihelion (from 2018 November 4 to 2018 November 7) of PSP. The magnetic-field data are provided by the FIELDS instrument suite (Bale et al. 2016). We use a merged-SCaM data set with magnetic-field resolution 293 Hz from fluxgate magnetometer (MAG) and search coil (SCM) measurements (Bowen et al. 2020c). The proton moments (density, velocity, and temperature) data and spacecraft position data are from the Solar Wind Electron Alpha Proton (SWEAP) experiment (Kasper et al. 2016; Case et al. 2020). We divide the data into one-hour intervals for calculations, and a total of 75 intervals are obtained. To reduce the possible influence of Alfvén ion-cyclotron waves (ACWs), which have been demonstrated to play an important role in solar wind turbulence in the inner heliosphere (e.g., Bowen et al. 2020b; Huang et al. 2020c), on our intervals, we search for intervals less affected by ACWs by two steps. First, those intervals whose magnetic-trace power spectrum exist as an obvious bump near the ion-cyclotron scale or ion-inertial scale are excluded. Then, we use the reduced magnetic helicity σ_m, which has been applied to identify the ACWs (He et al. 2011, 2015; Podesta & TenBarge 2012; Podesta 2013; Huang et al. 2020c), to determine the remaining suitable intervals. Specifically, signals with $\sigma_m < 0$ ($\sigma_m > 0$), nearly radial $\theta_{\rm RB}$ ($or\ \theta_{\rm VB}$), and $B_R > 0$ ($B_R < 0$) at near ion-cyclotron or ion-inertial scale can be considered as ACWs; here $\theta_{\rm RB}$ ($or\ \theta_{\rm VB}$) refers to the angle between the direction of the local mean magnetic field and the radial direction (or the solar wind velocity) and B_R is the radial component of magnetic field. Hence, we can inspect the distribution $\sigma_m(\theta_{\rm RB}, f)$ to determine whether ACWs are involved in a certain interval. The Morlet wavelet transform and Gaussian window are employed, respectively, to build the σ_m of the magnetic fluctuations and $\theta_{\rm RB}$ as in Podesta (2009) and He et al. (2011), then we can construct a distribution of $\sigma_m(\theta_{\rm RB}, f)$. In this way, a total of 22 intervals are finally chosen to perform our analysis. Meanwhile, we have checked the magnetic-field power spectral densities (PSDs) in different $\theta_{\rm RB}$ as shown in Figure 2(a) of Duan et al. (2021), and the results illustrate that the PSDs in all directions are well above the noise of the SCM and that in the magnetic-trace power spectrum there exists an obvious signature of the transition range for these 22 intervals. The average magnetic-field magnitude of 22 intervals is 87.1 ± 8.2 nT, the solar wind speed is 350.9 ± 30.1 km s^{-1}, the average Alfvén speed is 107.9 ± 13.2 km s^{-1}, and the proton inertial length is 13.0 ± 1.3 km.

Following the analysis method—five-point second-order SFs—introduced by Cho & Lazarian (2009), which is sensitive to steeper spectra and has been applied to reveal the anisotropy of turbulence at kinetic scales in several studies (e.g., Cerri et al. 2019; Wang et al. 2020; Duan et al. 2021), we perform five-point SFs on PSP observations in this study. The definition of the five-point SF is as follows:

$$\mathrm{SF}(\boldsymbol{l}; f) = \langle |[f(\boldsymbol{r} - 2\boldsymbol{l}) - 4f(\boldsymbol{r} - \boldsymbol{l}) + 6f(\boldsymbol{r}) - 4f(\boldsymbol{r} + \boldsymbol{l})) + f(\boldsymbol{r} + 2\boldsymbol{l})]/\sqrt{35}|^2 \rangle_{\boldsymbol{r}}, \quad (1)$$

where f can be the total magnetic field and its components, $\langle ... \rangle_{\boldsymbol{r}}$ represents the ensemble average (before averaging, the SFs of each one-hour interval are normalized to the square of the mean field strength over the interval $\langle |B|^2 \rangle$ to account for the possible various power levels due to the different intervals, and we refer to the normalized SFs as SFs throughout the paper unless stated otherwise), and $\boldsymbol{l} = \tau \cdot \boldsymbol{V}$ is the space displacement. According to Taylor's hypothesis, the spacecraft speed in the inner heliosphere may be too large to influence the estimation for spatial scale (e.g., Chhiber et al. 2019; Perez et al. 2021), so we use $\boldsymbol{V} = \boldsymbol{V}_{\rm local} - \boldsymbol{V}_{\rm sc}$ in our calculation, where $\boldsymbol{V}_{\rm local} = \boldsymbol{V}(\boldsymbol{r} - 2\boldsymbol{l}) + 4\boldsymbol{V}(\boldsymbol{r} - \boldsymbol{l}) + 6\boldsymbol{V}(\boldsymbol{r}) + 4\boldsymbol{V}(\boldsymbol{r} + \boldsymbol{l})) + \boldsymbol{V}(\boldsymbol{r} + 2\boldsymbol{l})]/16$ and $\boldsymbol{V}_{\rm sc}$ represents to the speed of spacecraft.

We project the SFs into the Cartesian coordinates system ($\hat{L}_{\perp}$, $\hat{l}_{\perp}$, $\hat{l}_{||}$) and spherical polar coordinates system (l, θ_B, $\phi_{\delta B_{\perp}}$) to analyze 3D properties of turbulence. We use the same local and physically motivated coordinate systems as Chen et al. (2012) and Wang et al. (2020). In the frame of reference, $\hat{l}_{||}$ represents the local magnetic-field direction $\boldsymbol{B}_{\rm local} = \boldsymbol{B}(\boldsymbol{r} - 2\boldsymbol{l}) + 4\boldsymbol{B}(\boldsymbol{r} - \boldsymbol{l}) + 6\boldsymbol{B}(\boldsymbol{r}) + 4\boldsymbol{B}(\boldsymbol{r} + \boldsymbol{l})) + \boldsymbol{B}(\boldsymbol{r} + 2\boldsymbol{l})]/16$, and $\hat{L}_{\perp}$ is the local perpendicular fluctuation direction along with $\delta\boldsymbol{B}_{\perp} = \boldsymbol{B}_{\rm local} \times [\delta\boldsymbol{B} \times \boldsymbol{B}_{\rm local}]$; finally, $\hat{l}_{\perp}$ completes the right-handed triad. And we use $L_{\perp} = \boldsymbol{l} \cdot \hat{L}_{\perp}$, $l_{\perp} = \boldsymbol{l} \cdot \hat{l}_{\perp}$, and $l_{||} = \boldsymbol{l} \cdot \hat{l}_{||}$ to represent the scales in the three directions, respectively. θ_B and $\phi_{\delta B_{\perp}}$ represent the angle between $\boldsymbol{B}_{\rm local}$ and $\boldsymbol{l}$, the angle between $\hat{L}_{\perp}$, and the

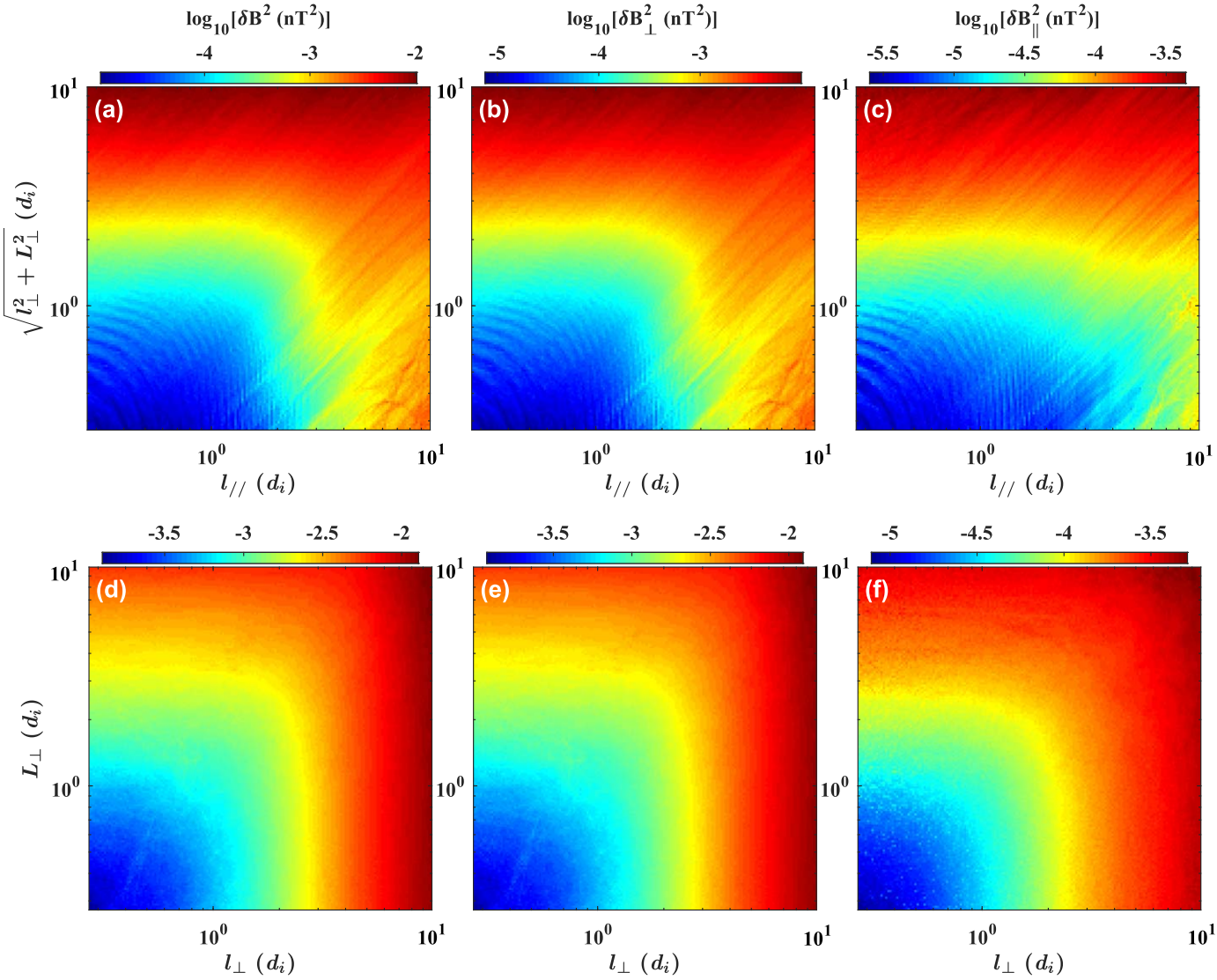

Figure 1. 2D SFs in ($l_{||}$, $\sqrt{l_\perp^2 + L_\perp^2}$) and ($l_\perp$, $L_\perp$) planes. The first, second, and third columns represent SFs of the total, perpendicular, and parallel magnetic-field fluctuations, respectively. The symbols ($l_{||}$, $l_\perp$, $L_\perp$) represent the spatial distances along the parallel, perpendicular, and displacement directions.

component of $\boldsymbol{l}$ perpendicular to $\boldsymbol{B}_{\rm local}$, respectively, and $l = |\boldsymbol{l}|$ represents the scale. The angles greater than 90° are reflected below 90° to improve scaling measurement accuracy (e.g., Chen et al. 2012).

3. Results

The binned SFs for the total magnetic field, perpendicular and parallel components in the ($l_{||}$, $\sqrt{l_\perp^2 + L_\perp^2}$) and ($l_\perp$, $L_\perp$) planes located at 151 logarithmically even spaced scales from $10^{-0.5} - 10^1$ ($\sim 0.3 - 10$)d_i, are shown in Figure 1. Each bin is required to have a minimum number of 1000 data points to ensure reliable results as in Chen et al. (2010) and Wang et al. (2020). One can clearly see the elongation along the parallel direction of the SFs' distributions from Figures 1(a)–(c), where $\sqrt{l_\perp^2 + L_\perp^2} > l_{||}$ for a same value of SF, indicating that the eddies are anisotropic with $k_\perp > k_{||}$ (e.g., Chen & Boldyrev 2017). Furthermore, the distribution and magnitude of SF($\boldsymbol{l}$; $B_\perp$) are comparable to that of SF($\boldsymbol{l}$; $\boldsymbol{B}$), thus, confirming the dominant contribution of perpendicular magnetic-field fluctuations to SFs. Besides, the elongation of SF($\boldsymbol{l}$; $B_\perp$) and SF($\boldsymbol{l}$; $\boldsymbol{B}$) shows a trend of decreasing as the scale increases but this trend is much weaker for SF($\boldsymbol{l}$; $B_{||}$). On the one hand, this signature indicates that the anisotropy is scale-dependent; on the other hand, it manifests that the anisotropy of the perpendicular magnetic-field fluctuations and the parallel magnetic-field fluctuations show different scale properties analogous to the results of MHD turbulence in Chen et al. (2012). In the ($l_\perp$, $L_\perp$) plane, both SF($\boldsymbol{l}$; $\boldsymbol{B}$) and SF($\boldsymbol{l}$; $B_\perp$) present a distribution of slight elongation along with $\hat{L}_\perp$ (Figures 1(d)–(e)), but SF($\boldsymbol{l}$; $B_{||}$) is nearly isotropic (Figure 1(f)). In short, the distribution of SF($\boldsymbol{l}$; $\boldsymbol{B}$) and SF($\boldsymbol{l}$; $B_\perp$) can be characterized by $l_{||} > L_\perp > l_\perp$, but it features as $l_{||} > L_\perp \approx l_\perp$ for SF($\boldsymbol{l}$; $B_{||}$).

To study the scale-dependent anisotropy more directly, we display the 1D SFs in Figures 2(a)–(c). The SFs in the three orthogonal directions are defined as follows:

$$\mathrm{SF}(L_\perp; f) = SF(L_\perp; f, 85^\circ < \theta_B < 90^\circ, 0^\circ < \phi_{\delta B_\perp} < 5^\circ), \quad (2)$$

$$\mathrm{SF}(l_\perp; f) = SF(l_\perp; f, 85^\circ < \theta_B < 90^\circ, 85^\circ < \phi_{\delta B_\perp} < 90^\circ), \quad (3)$$

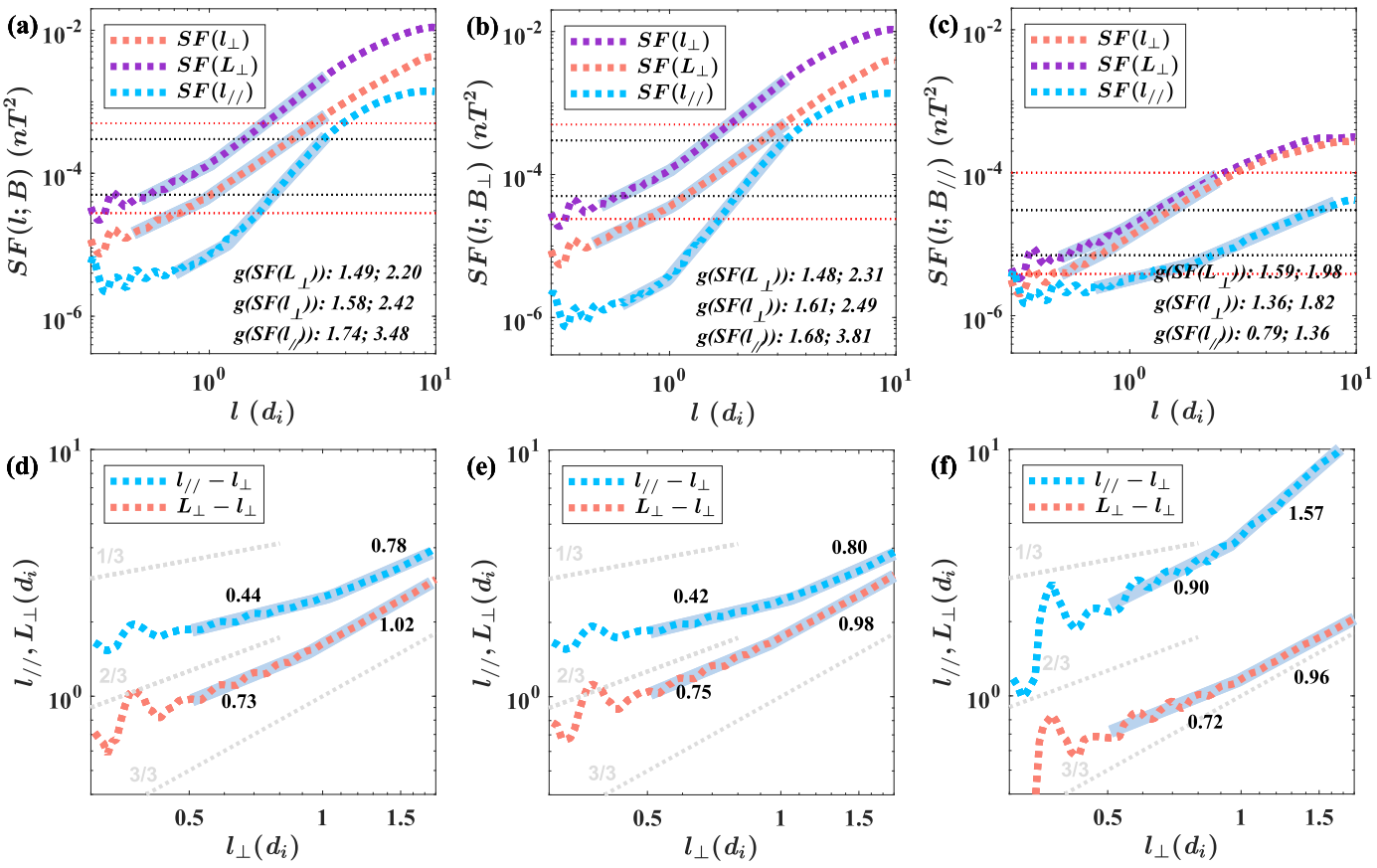

Figure 2. The upper panels (a)–(c) represents the 1D SFs vs. $L_\perp$, $l_\perp$ and $l_{||}$, and the lower panels (d)–(f) shows the relation between $L_\perp$, $l_\perp$, and $l_{||}$. In the upper panels, the horizontal dashed red lines indicate the range to calculate the wave-vector anisotropy and the black lines mark two values of SFs for 3D visualization. In the lower panel, three typical relations are presented as gray dotted lines for reference and lines marked with "3/3" represent isotropic relations. The bold gray transparent solid lines are our fitting lines. The first, second, and third columns represent the SFs of the total, perpendicular, and parallel magnetic-field fluctuations, respectively.

$$\mathrm{SF}(l_{||}; f) = SF(l_{||}; f, 0^\circ < \theta_B < 5^\circ, 0^\circ < \phi_{\delta B_\perp} < 90^\circ). \quad (4)$$

As one can see, the relation of $\mathrm{SF}(l_\perp) > \mathrm{SF}(L_\perp) > \mathrm{SF}(l_{||})$ is well satisfied above 0.5 d_i (the large disturbance below ~0.4 d_i may come from the noise of reaction wheels setting on the spacecraft which contaminates the power spectra around 20 ~ 30 Hz e.g., Duan et al. 2021) for SF($\boldsymbol{B}$) and SF($B_\perp$), which verifies the 3D anisotropy of the total and the perpendicular magnetic-field fluctuations again. However, for SF($B_{||}$), it presents as $\mathrm{SF}(l_\perp) SF \approx (L_\perp) > \mathrm{SF}(l_{||})$. We can relate the power-law index of the SFs, g, to the power spectral index, α ($E(k) \sim k^\alpha$), by $\alpha = -(g+1)$ (e.g., Chen et al. 2010). Due to the strong power anisotropy, when the perpendicular SFs reach the noise, the parallel SFs are still in the ion-to-electron scales, therefore, we can only perform our fitting procedure on different ranges of scale. Continuous power-law functions with two spectral ranges are chosen as our fitting functions, which forms as follows:

$$\log_{10} SF = \begin{cases} g_k \log_{10} l + b1, & l_{\min} \leqslant l \leqslant l_0 \\ g_t \log_{10} l + b2, & l_0 < l \leqslant l_{\max} \end{cases} (g_i \log_{10} l_0 + \mathrm{b1} \equiv g_t \log_{10} l_0 + b2), \quad (5)$$

here $l_{\min} \leqslant l \leqslant l_{\max}$ is the chosen fitting range, g_k, g_t are the fitting power-law indices of *SFs* in the ion-to-electron scales and the transition range, and $b1$, $b2$, l_0 are other fitting cofficients. Optimizing the residuals, we get the two power-law indices g_k and g_t. The results are displayed in Figures 2(a)–(c). By equating the SFs in the three directions, one can infer the wave-vector anisotropy scalings between $L_\perp$, $l_\perp$, and $l_{||}$, and a similar fitting procedure is applied to the results, which are shown in Figures 2(d)–(f). The variance of the residuals is from 0.01 to 0.02 in all panels of Figure 2. For SF($\boldsymbol{B}$), we get $\alpha_t(\mathrm{SF}(L_\perp)) \approx -3.20$, $\alpha_t(\mathrm{SF}(l_\perp)) \approx -3.42$ and $\alpha_t(\mathrm{SF}(l_{||})) \approx -4.48$ in the transition range and $\alpha_k(\mathrm{SF}(L_\perp)) \approx 2.49$, $\alpha_k(\mathrm{SF}(l_\perp)) \approx 2.58$ and $\alpha_k(\mathrm{SF}(l_{||})) \approx 2.74$ (Figure 2(a)) in the ion-to-electron scales. The results extend the results of Duan et al. (2021) and indicate the existence of a steeper transition range in the three directions of $\hat{L}_\perp$, $\hat{l}_\perp$ and $\hat{l}_{||}$. The scalings as shown in Figure 2(d) are $l_{||} \propto {l_\perp}^{0.44}$ and $L_\perp \propto {l_\perp}^{0.73}$ in the ion-to-electron scales, $l_{||} \propto {l_\perp}^{0.78}$ and $L_\perp \propto {l_\perp}^{1.02}$ in the transition range. These results elucidate that the wave-vector anisotropy scalings of both $l_{||}$ and $l_\perp$, $L_\perp$ and $l_\perp$ vary from the ion-to-electron scales to the transition range, which have never been reported before. As expected, both the spectral indices (Figure 2(b)) and wave-vector anisotropy scalings (Figure 2(e)) of SF($B_\perp$) are very similar to those of SF($\boldsymbol{B}$). However, the situation becomes very different for SF($B_{||}$). The discrepancies

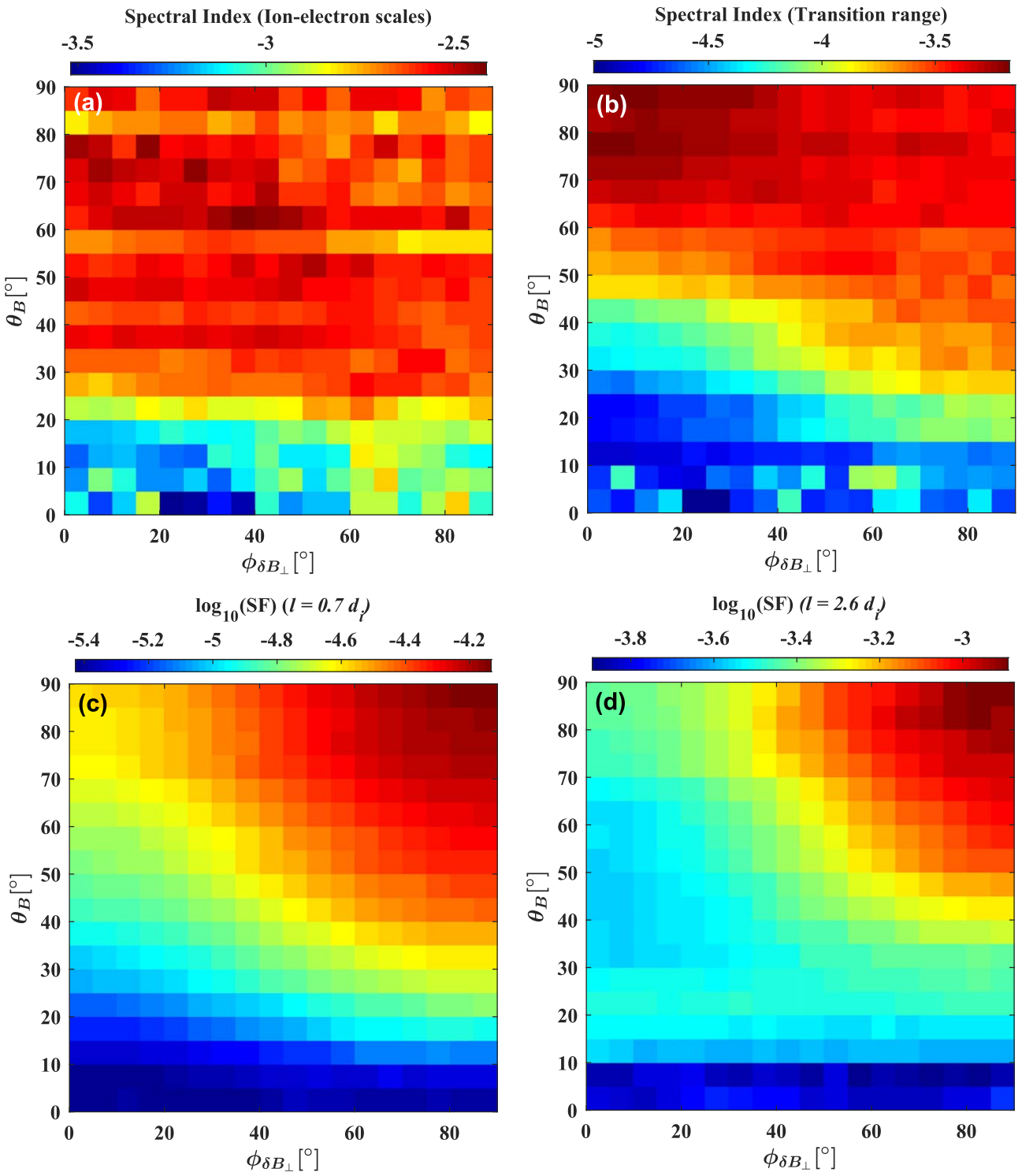

Figure 3. The upper panel: distributions of spectral indices at (a) the ion-to-electron scales and (b) the transition range in the ($\phi_{\delta B_\perp}$, θ_B) plane. The lower panel: SFs at (c) 0.7 d_i and (d) 2.6 d_i as a function of $\phi_{\delta B_\perp}$ and θ_B.

between α_k and α_t for SF($B_{||}$) in the three directions are smaller than those for SF($\boldsymbol{B}$) and SF($B_\perp$), which can be seen in Figure 2(c). In the meanwhile, the scalings between $l_{||}$ and $l_\perp$ are also much different (Figure 2(f)). However, the scalings of $L_\perp \propto l_\perp^{0.72}$ and $L_\perp \propto l_\perp^{0.96}$ (Figure 2(f)) are very similar to those for SF($\boldsymbol{B}$) and SF($B_\perp$).

By binning the SF($\boldsymbol{l}$, $\boldsymbol{B}$) in the plane ($\phi_{\delta B_\perp}$, θ_B) and applying the same fitting procedure as in Figures 2(a)–(b), we obtain the anisotropy of the spectral indices shown in Figure 3(a) for the ion-to-electron scales and Figure 3(b) for the transition range. The variance of the residuals is no more than 6.2% in the two panels. The spectral indices steepening toward small θ_B

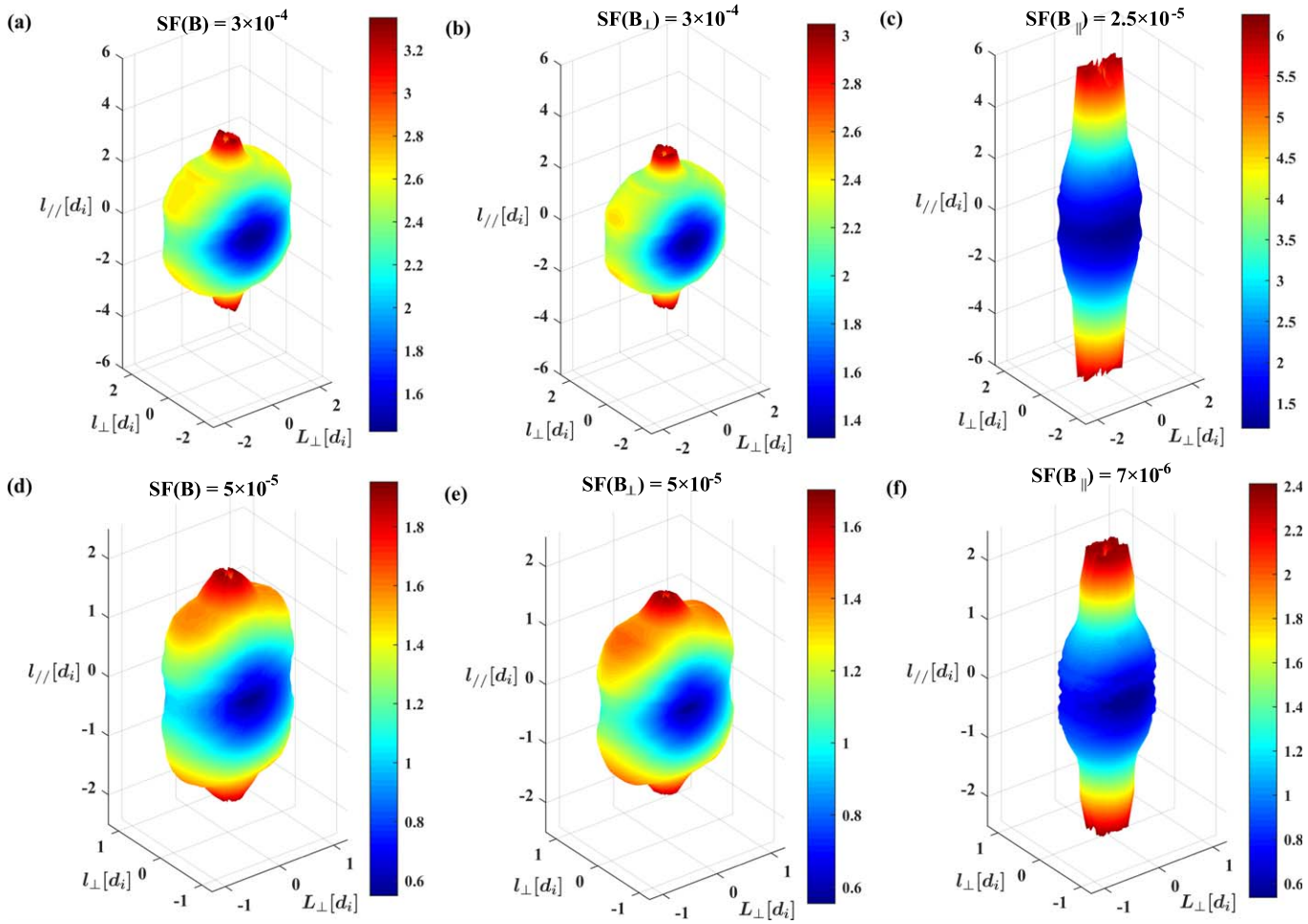

Figure 4. The first, second, and third columns represent isosurfaces of SFs for the total, the perpendicular, and the parallel magnetic-field fluctuations. The upper panel shows isosurfaces at higher values of SF, and smaller values in the lower panel. These SFs are marked with black dashed lines on Figures 2(a)–(c). The colors indicate distances from the origin to help in visualizing the anisotropy.

(Horbury et al. 2008) can be seen in both ranges, but there appears to be little variation with $\phi_{\delta B_\perp}$ at large θ_B. For each angle bin, the fits to the SFs are evaluated at 0.7 d_i (at ion-to-electron scales) and 2.6 d_i (at transition range) to give the 3D power anisotropy, which are shown in Figures 3(c)–(d). It can be seen that the power increases with both θ_B and $\phi_{\delta B_\perp}$ at these two scales, indicating 3D anisotropy, and seems to peak near $\theta_B = 90°$.

Figure 4 presents a 3D visualization of the turbulence eddies at two selected SF values which are indicated by the two horizontal dashed black lines in Figures 2(a)–(c) for SF($\boldsymbol{B}$), SF($B_\perp$) and SF($B_\parallel$). The three upper panels (Figures 4(a)–(c)) correspond to larger values of SF, and the results of the smaller values are shown in the three lower panels (Figures 4(d)–(f)). Because the angle ranges of $\phi_{\delta B_\perp}$ and θ_B are both from 0° to 90°, we obtain the other seven octants by reflecting the isosurface in the first quadrant as in Chen et al. (2012), Verdini et al. (2018), and Wu et al. (2019). The relation of $l_\parallel > L_\perp > l_\perp$ for SF($\boldsymbol{B}$) and SF($B_\perp$) and $l_\parallel > L_\perp \approx l_\perp$ for SF($B_\parallel$) can be clearly identified in the two selected values. In addition, the much elongated structure of magnetic-field fluctuations in the parallel direction can be observed in Figures 4(c) and (f).

4. Discussions and Conclusions

In the present study, we investigate the anisotropy of solar wind turbulence at kinetic scales in the inner heliosphere using PSP observations. By constructing the five-point second-order SFs, we display the 3D anisotropies, wave-vector anisotropy scalings, and structures of solar wind turbulence for the total, perpendicular, and parallel magnetic-field fluctuations. It shows that solar wind turbulence is elongated in the direction parallel to the background magnetic field for the total and the perpendicular magnetic-field fluctuations, and much elongated for the parallel magnetic-field fluctuations. In the perpendicular plane, anisotropic distributions can only be observed for the total and the perpendicular magnetic-field fluctuations, which is similar to the observational results in the Earth's magnetosheath (Wang et al. 2020). Furthermore, the anisotropic scalings for the total magnetic-field fluctuations behave as $l_\parallel \propto {l_\perp}^{0.78}$ and $L_\perp \propto {l_\perp}^{1.02}$ in the transition range, $l_\parallel \propto {l_\perp}^{0.44}$ and $L_\perp \propto {l_\perp}^{0.73}$ in the ion-to-electron scales.

In a recent work, Duan et al. (2021) reported different 2D wave-vector anisotropy scalings at the transition range and ion-to-electron scales using PSP's first perihelion data. Specifically, the anisotropic scalings featured as $k_\parallel \propto k_\perp^{0.71\pm0.17}$ at the transition range and $k_\parallel \propto k_\perp^{0.38\pm0.09}$ at the ion-to-electron scales, and they attributed these features to KAW turbulence. The scalings of $l_\parallel \propto l_\perp^{0.78}$ and $l_\parallel \propto l_\perp^{0.44}$ in these two ranges observed in our work are similar to their results. A mild deviation exists between them, which may derive from our analysis of 3D anisotropic properties rather than 2D anisotropy, hence $\hat{l}_\perp$ is the only perpendicular direction and cannot represent the collective

characteristics of all perpendicular directions. Another reason could be due to differences in data sets. If we take the scaling between $L_\perp$ and $l_\perp$ as consideration, the scalings of $l_\parallel \propto l_\perp^{0.78}$ and $L_\perp \propto l_\perp^{1.02}$ at the transition range is much similar to the results at the kinetic scales of Wang et al. (2020), in which the scalings factor as $l_\parallel \propto l_\perp^{0.71}$ and $L_\perp \propto l_\perp^{1.08}$. However, the scalings of $l_\parallel \propto l_\perp{}^{0.44}$ and $L_\perp \propto l_\perp{}^{0.73}$ in the ion-to-electron scales has never been reported before.

The scaling of $l_\parallel \propto l_\perp^{0.71}$ at the transition range is different from traditional critical-balanced KAW turbulence of $k_\parallel \propto k_\perp^{1/3}$ (e.g., Howes et al. 2008; Schekochihin et al. 2009), but is close to the theoretical prediction of $k_\parallel \propto k_\perp^{2/3}$ from Boldyrev & Perez (2012), and is also in the range from $k_\parallel \propto k_\perp^{2/3}$ to $k_\parallel \propto k_\perp$ from Boldyrev & Loureiro (2019). However, the spectral indices predicted by both models are larger than our observations. Specifically, the perpendicular spectral index $-8/3$ and the parallel spectral index $-7/2$ predicted by Boldyrev & Perez (2012) are larger than -3.42 and -4.48 (Figure 2(a)) in our observations, respectively. In the latter model, the perpendicular spectral index ranging from $-8/3$ to -3 deduced by Boldyrev & Loureiro (2019) is also not consistent with our results. We note that Boldyrev & Perez (2012) assumed extremely extended sheet-like structures with $L_\perp \gg l_\perp$, but the scaling of $L_\perp \propto l_\perp^{1.08}$ in the perpendicular plane seems to deviate from this assumption, which may account for the differences in spectral indices. In the latter model, Boldyrev & Loureiro (2019) hold the viewpoint that magnetic reconnection may prevent KAW turbulence from forming extended sheet-like structures (see also in Loureiro & Boldyrev 2017; Mallet et al. 2017; Mallet 2020) which could explain this deviation to some extent, but the differences between this model and our observation still need additional theories to account for everything. This scaling of $l_\parallel \propto l_\perp^{0.71}$ also corresponds to $\alpha = 1.34$ in the framework of the model by Landi et al. (2019), but the predicted spectral indices in both the parallel (-2.78) and the perpendicular (-3.28) directions are larger than our observations, too. Besides this, simulations from Cerri et al. (2019) showed the same wave-vector anisotropy scaling of $k_\parallel \propto k_\perp^{2/3}$. In their three kinds of simulations, two of them displayed perpendicular spectral indices near $-7/2$ which seems to have a great consensus with our results, but the corresponding parallel spectral indices are much smaller. The other possible reasons for the steep spectra at the transition range may come from the helicity barrier (e.g., Meyrand et al. 2021; Squire et al. 2021) and the dissipative effects (e.g., Bowen et al. 2020a).

In the ion-to-electron scales, Duan et al. (2021) ascribe the 2D anisotropic scaling of $l_\parallel \propto l_\perp^{0.38\pm0.09}$ to the critical-balanced KAW turbulence with a scaling of $k_\parallel \propto k_\perp^{1/3}$. However, if we take the anisotropy in the plane perpendicular to $\boldsymbol{B}_{\rm local}$ into account, we obtain $l_\parallel \propto l_\perp^{0.44}$ and $L_\perp \propto l_\perp^{0.73}$, which is reminiscent of the distinguished dynamic alignment cascade model (Boldyrev 2006) with scalings of $l_\parallel \propto l_\perp^{1/2}$ and $L_\perp \propto l_\perp^{3/4}$ at MHD scales. This may indicate that another cascade exists before the electron-dissipation range (e.g., Sahraoui et al. 2020; Huang et al. 2021).

As only a theoretical prediction for 3D wave-vector anisotropy scalings for the MHD scales exist (e.g., Boldyrev 2006; Mallet & Schekochihin 2017) but no such prediction exists for KAW turbulence, our observation may shed light on 3D model constructions of kinetic-scale turbulence. However, compared to the results of Wang et al. (2020), our observations elucidate that the transition range may have influenced the anisotropic properties in the ion-to-electron scales. Hence, a more detailed comparation in similar plasma environment needs to be studied in the future.

This work was supported by the National Natural Science Foundation of China (41874191, 42074196, 41925018, 41874200) and the National Youth Talent Support Program. The data sets analyzed in the present study are publicly available from the NASA's Space Physics Data Facility (SPDF) at https://spdf.gsfc.nasa.gov/pub/data/psp/.

ORCID iDs

J. Zhang https://orcid.org/0000-0001-5111-2609
S. Y. Huang https://orcid.org/0000-0002-3595-2525
J. S. He https://orcid.org/0000-0001-8179-417X
T. Y. Wang https://orcid.org/0000-0003-3072-6139
K. Jiang https://orcid.org/0000-0001-7889-0507
R. T. Lin https://orcid.org/0000-0003-4012-9418

References

Arzamasskiy, L., Kunz, M. W., Chandran, B. D., & Quataert, E. 2019, ApJ, 879, 53
Bale, S. D., Goetz, K., Harvey, P. R., et al. 2016, SSRv, 204, 49
Boldyrev, S. 2006, PhRvL, 96, 115002
Boldyrev, S., & Loureiro, N. F. 2019, PhRvR, 1, 012006
Boldyrev, S., & Perez, J. C. 2012, ApJL, 758, L44
Bowen, T. A., Bale, S. D., Bonnell, J. W., et al. 2020c, JGRA, 125, e27813
Bowen, T. A., Mallet, A., Bale, S. D., et al. 2020a, PhRvL, 125, 025102
Bowen, T. A., Mallet, A., Huang, J., et al. 2020b, ApJS, 246, 66
Bruno, R., & Carbone, V. 2005, LRSP, 2, 4
Bruno, R., & Carbone, V. 2013, LRSP, 10, 2
Bruno, R., Trenchi, L., & Telloni, D. 2014, ApJL, 793, L15
Case, A. W., Kasper, J. C., Stevens, M. L., et al. 2020, ApJS, 246, 43
Cerri, S. S., Grošelj, D., & Franci, L. 2019, FrASS, 6, 64
Chen, C. H., & Boldyrev, S. 2017, ApJ, 842, 122
Chen, C. H. K., Bale, S. D., Bonnell, J. W., et al. 2020, ApJS, 246, 53
Chen, C. H. K., Horbury, T. S., Schekochihin, A. A., et al. 2010, PhRvL, 104, 255002
Chen, C. H. K., Mallet, A., Schekochihin, A. A., et al. 2012, ApJ, 758, 120
Chhiber, R., Usmanov, A. V., Matthaeus, W. H., Parashar, T. N., & Goldstein, M. L. 2019, ApJS, 242, 12
Cho, J., & Lazarian, A. 2009, ApJ, 701, 236
Coleman, P. J., Jr 1968, ApJ, 153, 371
Comişel, H., Narita, Y., & Motschmann, U. 2014, NPGeo, 21, 1075
Duan, D., He, J., Bowen, T. A., et al. 2021, ApJL, 915, L8
Fox, N. J., Velli, M. C., Bale, S. D., et al. 2016, SSRv, 204, 7
Grošelj, D., Mallet, A., Loureiro, N. F., & Jenko, F. 2018, PhRvL, 120, 105101
He, J., Marsch, E., Tu, C., Yao, S., & Tian, H. 2011, ApJ, 731, 85
He, J., Tu, C., Marsch, E., & Yao, S. 2012, ApJL, 745, L8
He, J., Wang, L., Tu, C., Marsch, E., & Zong, Q. 2015, ApJL, 800, L31
Horbury, T. S., Forman, M., & Oughton, S. 2008, PhRvL, 101, 175005
Horbury, T. S., Wicks, R. T., & Chen, C. H. K. 2012, SSRv, 172, 325
Howes, G. G., Bale, S. D., Klein, K. G., et al. 2012, ApJL, 753, L19
Howes, G. G., Cowley, S. C., Dorland, W., et al. 2008, JGRA, 113, A05103
Huang, S., Sahraoui, F., Deng, X., et al. 2014, ApJL, 789, L28
Huang, S. Y., Hadid, L. Z., Sahraoui, F., Yuan, Z. G., & Deng, X. H. 2017, ApJL, 836, L10
Huang, S. Y., & Sahraoui, F. 2019, ApJ, 876, 138
Huang, S. Y., Sahraoui, F., Andrés, N., et al. 2021, ApJL, 909, L7
Huang, S. Y., Wang, Q. Y., Sahraoui, F., et al. 2020b, ApJ, 891, 159
Huang, S. Y., Zhang, J., Sahraoui, F., et al. 2020a, ApJL, 898, L18
Huang, S. Y., Zhang, J., Sahraoui, F., et al. 2020c, ApJL, 897, L3
Huang, S. Y., Zhou, M., Sahraoui, F., et al. 2012, GeoRL, 39, L11104
Kasper, J. C., Abiad, R., Austin, G., et al. 2016, SSRv, 204, 131
Kiyani, K. H., Chapman, S. C., Sahraoui, F., et al. 2013, ApJ, 763, 10
Lacombe, C., Alexandrova, O., & Matteini, L. 2017, APJ, 848, 45
Landi, S., Franci, L., Papini, E., et al. 2019, arXiv:1904.03903
Loureiro, N. F., & Boldyrev, S. 2017, ApJ, 850, 182
Mallet, A. 2020, JPlPh, 86, 905860301
Mallet, A., & Schekochihin, A. A. 2017, MNRAS, 466, 3918
Mallet, A., Schekochihin, A. A., & Chandran, B. D. G. 2017, MNRAS, 468, 4862

Meyrand, R., Squire, J., Schekochihin, A. A., & Dorland, W. 2021, JPlPh, 87, 535870301
Osman, K. T., Wan, M., Matthaeus, W. H., Weygand, J. M., & Dasso, S. 2011, PhRvL, 107, 165001
Oughton, S., Matthaeus, W. H., Wan, M., & Osman, K. T. 2015, RSPTA, 373, 20140152
Parashar, T. N., Oughton, S., Matthaeus, W. H., & Wan, M. 2016, ApJ, 824, 44
Perez, J. C., Bourouaine, S., Chen, C. H., & Raouafi, N. E. 2021, A&A, 650, A22
Podesta, J. J. 2009, ApJ, 698, 986
Podesta, J. J. 2013, SoPh, 286, 529
Podesta, J. J., & TenBarge, J. M. 2012, JGRA, 117, A10106
Roberts, O. W., Narita, Y., Nakamura, R., Vörös, Z., & Gershman, D. 2019, FrP, 7, 184
Sahraoui, F., Belmont, G., & Goldstein, M. L. 2012, ApJ, 748, 100
Sahraoui, F., Belmont, G., Rezeau, L., et al. 2006, PhRvL, 96, 075002
Sahraoui, F., Goldstein, M. L., Belmont, G., Canu, P., & Rezeau, L. 2010, PhRvL, 105, 131101
Sahraoui, F., Goldstein, M. L., Robert, P., & Khotyaintsev, Y. V. 2009, PhRvL, 102, 231102
Sahraoui, F., Hadid, L., & Huang, S. Y. 2020, RvMPP, 4, 1
Sahraoui, F., Huang, S. Y., Belmont, G., et al. 2013, ApJ, 777, 15
Schekochihin, A. A., Cowley, S. C., Dorland, W., et al. 2009, ApJS, 182, 310
Squire, J., Meyrand, R., Kunz, M. W., et al. 2021, arXiv:2109.03255
Tu, C. Y., & Marsch, E. 1995, SSRv, 73, 1
Verdini, A., Grappin, R., Alexandrova, O., & Lion, S. 2018, ApJ, 853, 85
Wang, T., He, J., Alexandrova, O., Dunlop, M., & Perrone, D. 2020, ApJ, 898, 91
Wang, X., Tu, C., & He, J. 2019, ApJ, 871, 93
Wu, H., Tu, C., Wang, X., He, J., & Wang, L. 2019, ApJL, 883, L9
Zhao, J. S., Voitenko, Y. M., Wu, D. J., & Yu, M. Y. 2016, JGRA, 121, 5